

Iterative Refinement of Arbitrary Micro-Optical Surfaces

MEAGAN PLUMMER,^{1,3} STEPHEN TAYLOR,⁴ MATTHEW MARSHALL,^{2,3}
DAVID BROWN,⁴ ROBERT LEONARD,⁵ SETH HYRA,⁶ AND SPENCER
OLSON^{6,*}

¹*Optical Science & Engineering Program, University of New Mexico, Albuquerque, NM 87131*

²*Department of Physics and Astronomy, University of New Mexico, Albuquerque, NM 87131*

³*Universities Space Research Association*

⁴*National Research Council, National Academies of the Sciences*

⁵*Space Dynamics Laboratory, Quantum Sensing & Timing, North Logan, UT 84341, USA*

⁶*Air Force Research Laboratory, Kirtland Air Force Base, NM 87117, USA*

*spencer.olson.2@afrl.af.mil

Abstract:

We introduce an adaptive optical refinement method enabling ultra-precise micro-milling of arbitrary surfaces. Through repeated iteration, our method reduces surface error without requiring significant specific surface engineering. This remediates the long sample preparation times and lack of refinement capability that previously reported methods suffer from. The iterative refinement milling method was used to produce spherical mirrors with small radii of curvature and low surface roughness for use in micro Fabry-Perot cavities. We demonstrate the use of this adaptive process to produce a variety of arbitrary surface geometries on both optical fiber tips as well as optical flats. We additionally discuss our capability to apply iterative refinement milling adaptively to various materials, including to construct GRIN lenses.

1. Introduction

The development of advanced micro-milling techniques has contributed to the ubiquity of high finesse optical cavities, including fiber Fabry-Perot cavities (FFPCs), in applications across many disciplines, from sensing to information [1–5]. FFPCs are micro-optical resonators made by shaping the tips of optical fibers such that stable cavities can be formed in the gap between two opposing tips [6]. FFPCs are well-suited for strong atom-cavity coupling due to their small mode-volume, inherent fiber coupling, and open-access geometry. However, traditional polishing techniques are insufficient to form mirrors with the small radii of curvature required to form a stable FFPC [6]. Several techniques have been developed to machine concave surfaces on optical fibers, including chemical etching [7], focused ion beam milling [8], and laser ablation [9]. Of these, laser ablation has been the most promising to produce sufficiently low roughness surfaces to enable high finesse cavities [6].

Laser ablation milling is typically performed by applying a single pulse from a CO₂ laser to the facet of an optical fiber, creating a Gaussian-like indentation on the fiber [9]. A drawback to this technique is that the size and shape of the indentation is limited by the transverse mode of the ablating beam [10]. This constraint can be removed by applying a series of weak pulses to spatially separate points, or dots, across the fiber surface [11]. This technique, sometimes referred to as *dot-milling*, may be used to mill near-arbitrary surface geometries.

A significant drawback of the dot-milling technique is that the power, duration, and location of each spatially separate pulse must be tuned precisely to minimize error in the milled surface [11]. The parameter space which must be explored to optimize this milling process is extensive. These parameters are highly coupled, as the indentation formed by each pulse overlaps with indentations of neighboring pulses. Furthermore, the efficacy of a laser pulse to cause material removal is significantly affected by small deviations in the local surface shape where the laser interacts. Additionally, changes in environmental conditions can alter the laser-surface interaction and affect material removal. Moreover, learning by iterating through parameters applied to a known starting surface requires samples to be (re)polished and/or replaced frequently. Finally, such an optimized process will need to be re-engineered whenever the target surface geometry or the target material changes.

In this paper we present an adaptive milling method where multiple iterations hone the surface shape and asymptotically correct for surface errors. The primary effect of this approach is that specific optimization of the temporal and spatial milling pattern is not necessary. Furthermore, this approach can be easily applied to varying materials and surface geometries, provided a few engineering restrictions are met. Effectively, our process can be described by a feedback loop iteratively integrated with a dot-milling technique, superficially de-coupling the complexities of material physics and laser milling to achieve an optimized, error reduced, target surface.

2. Surface Quality as a Figure of Merit

As the techniques presented in this paper allow for a variety of functional forms for the target surface, the actual performance of the milled surface will ultimately depend on the specific application. Nevertheless, as a technique to apply generically to optical surfaces and for the scope of this paper, we simply focus on statistics of the measured difference of the milled surface to the desired functional form. This includes both full surface, macroscopic geometric deviations, as well as surface roughness.

As an example of this simple metric for evaluating milled-surface quality, consider the surfaces used to create FFPCs. A clear defining measure of quality for FFPCs is their finesse, an indicator of the sharpness of the etalon interference fringes and directly proportional to the single-atom cooperativity [12], as related to cavity quantum electrodynamics (cQED). While often measured in terms of free spectral range divided by the full width half maximum (FWHM) of the resonant

peaks, the finesse of a cavity, \mathcal{F} , can be represented solely as dependent on losses, \mathcal{L} , in the cavity via [13]

$$\mathcal{F}(\mathcal{L}) = \frac{\pi}{2 \sin^{-1} \left(\frac{1 - \sqrt{1 - \mathcal{L}}}{2 \sqrt[4]{1 - \mathcal{L}}} \right)}. \quad (1)$$

One can then determine the highest potential finesse of a system in terms of its most limiting loss source, assuming that the worst loss source is much more significant than others. The primary loss mechanisms in FFPCs are mode clipping, absorption, transmission, and surface scattering. For many geometries, it is relatively straight forward to minimize clipping by increasing mirror size, and in the case where the cavity mirror diameters are $\geq 3 \times$ the FWHM of the transverse cavity mode at the mirror surface, clipping losses become negligible (on the order of 0.004 ppm). Transmission and absorption losses are dictated by the quality of the reflective coating applied to the cavity mirrors, something outside the purview of the present discussion. Additional impacts of coating and/or annealing on final surface roughness are also out of scope of the present paper. As such, the best figure of merit connecting fabrication quality to cavity finesse is the optical surface roughness. The root-mean-square (RMS) surface roughness value, σ , can be directly connected to a scattering loss for a given wavelength, λ , by [14]

$$\mathcal{L}_s = 1 - e^{-\left(\frac{4\pi\sigma}{\lambda}\right)^2} \approx \left(\frac{4\pi\sigma}{\lambda}\right)^2, \quad (2)$$

and therefore to a scattering limited finesse $\mathcal{F}(\mathcal{L}_s)$, see Fig.1.

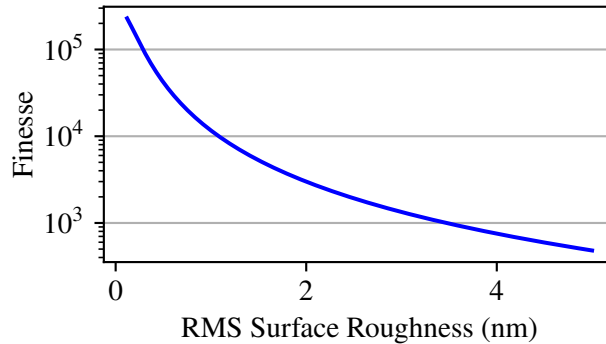


Fig. 1. Scattering limited finesse for RMS surface roughness from 0 to 5 nm for a nominal confocal cavity design with 1 mm radius of curvature (ROC).

From Eqs. 1 and 2, order of magnitude relations can be made between surface roughness and scattering limited finesse. For instance, taking a confocal cavity configuration with millimeter ROC, a surface roughness $\sigma = 1$ nm leads to $\mathcal{L} \approx 520$ ppm and $\mathcal{F} \approx 11,000$, whilst a $\sigma = 0.5$ nm leads to $\mathcal{L} \approx 130$ ppm and $\mathcal{F} \approx 40,000$. Within the context of cQED, the strong coupling regime occurs for single atom cooperativity > 1 , where cooperativity is given by [15]

$$\eta = \frac{6}{\pi^3} \frac{\mathcal{F} \lambda^2}{w_0^2} \quad (3)$$

In this example, the strong coupling regime is achieved when $\mathcal{F} \gtrsim 1,000$, and therefore when surface roughness $\sigma \leq 3.38$ nm. Different applications will imply different finesse and

atom cooperativity requirements, similarly setting bounds for maximum surface roughness. Cooperativities in excess of 100, deep within the strong coupling regime, correspond in our example system to a confocal millimeter cavity finesse of $\mathcal{F} = 110,000$ and a surface roughness $\sigma \leq 0.27$ nm.

To note, atom cooperativity may also be improved by reducing mode volume (proportional to the mode radius, w_0), as can be achieved through approaching the concentric regime. This will not directly impact the finesse, though clipping loss considerations will drive a requirement for larger radii mirrors to maintain a finesse commensurate with a desired atom cooperativity. The near concentric regime can therefore allow for higher atom cooperativities with a lower finesse, and thus a relaxed constraint on surface roughness. Surface roughness remains the limiting manufacturing parameter for both finesse and atom cooperativity, however, and as such is our figure of merit when assessing mill quality.

Minimization of macroscopic RMS deviations from a desired target surface also represent mill quality, indicating the degree of control over final milled surface geometry. The impacts of these surface errors are more specific to target geometry and application, and a thorough mode analysis for all milled structures is beyond the scope of this paper. Values for overall surface RMS will be provided as additional figures of merit for various milled geometries, and compared with those achieved by other fabrication methods.

3. Iterative Refinement Milling

Iterative refinement milling involves successive milling operations over a given surface to minimize overall error between the current measured surface and the final target surface. This error, measured using an optical profilometer, is input into a proportional feedback loop, where a set of laser pulse parameters are calculated to minimize the error. These corrective laser pulses are applied using a tightly integrated CO₂ laser system. The resulting surface feeds back into the refinement loop, where the new error is measured. This process is repeated, resulting in asymptotically reduced surface error, see Fig. 3.

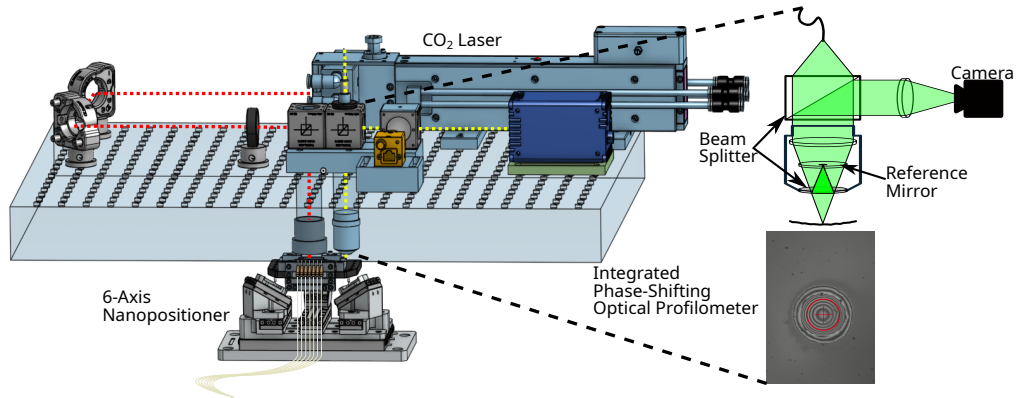


Fig. 2. Schematic of the laser milling system, showing the tight integration between the beam path for the laser ablation and the optical profilometer.

3.1. Theory of Operation

The target surface is established by a user-defined function which is called by the refinement code. These surfaces are mapped to a hexagonal grid of equidistant points which set locations for individual mill pulses. The choice of grid spacing between points, δr , impacts the mill quality and speed. We additionally shift the grid by a random fraction of δr between each mill

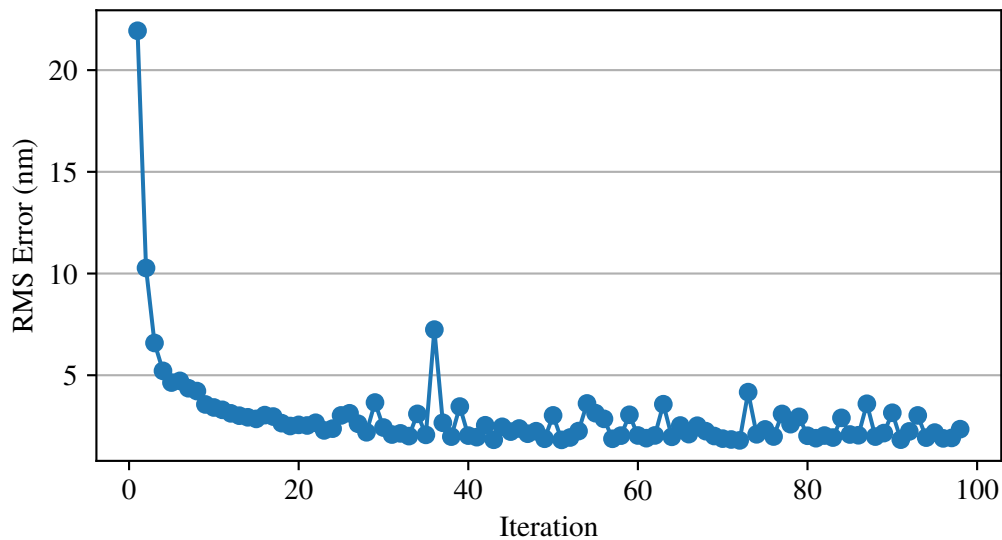


Fig. 3. Fixed RMS error rapidly declines during the first few iterations of a 1 mm ROC spherical surface. As the milled surface converges towards the targeted surface, the fixed RMS error continues a slow and steady decline. After approximately 25 iterations (dependent on the geometry of the target surface), we reach the limits of the milling precision, and RMS error begins to vary about a steady-state value. Providing an exit condition for our mill code enables consistent achievement of low RMS results. This example is characteristic of milling behavior.

iteration to prevent accumulation of grid structured systematic error. We have demonstrated milling spherical surfaces, multiple closely positioned spherical surfaces, and conical axicon surfaces, as discussed in Sec. 4.

We have additionally developed a simulated version of our custom laser mill code. This enables rapid trial and implementation of code improvements and new target surface geometries before deployment to the hardware. Trial arbitrary surfaces can be tested on the simulation to identify any required major alterations to milling parameters or surface definition before attempting destructive testing. This additionally allows for distinction between physical and algorithmic issues in milling.

Our system possess insufficient delivered power to produce clean ablation, and is observed to re-deposit material near the mill site. Our iterative method removes the necessity for clear understanding of the surface light-matter interactions, however, and can accommodate for these effects. Iterative refinement milling is adaptable to various power regimes of ablative laser milling.

The function of our iterative refinement technique relies upon the ability to reduce errors in proportion with the amount of material removed during milling. Sources of milling error can therefore be appropriately sorted into two categories: *constant errors* and *proportional errors*, where proportional errors are strongly correlated with the volume of material removed. Proportional errors dominate milling error during the initial iterations. During each iteration, a set of laser pulses removes a volume of material which is proportional to the difference between the target surface and the current surface. Consequently, less volume is removed during subsequent iterations, thereby reducing the proportional errors. This process continues until the milling error arising from proportional error sources are commensurate with the milling error from constant

error sources.

The milling apparatus, see Fig. 2 has been designed to minimize both constant and proportional errors. In the following sections, we will address each source of error separately, as well as feedback stability considerations.

3.2. Proportional Errors

Proportional errors limit the rate of convergence while maintaining feedback stability (we will discuss stability in Sec. 3.4). Indeed, in the absence of proportional errors, we could achieve minimum error through a single dot-milling iteration. Proportional errors include calibration error, pulse duration noise, and laser power noise.

3.2.1. Calibration Error

Before milling, the relationship between CO₂ laser pulse parameters and the parameters which describe the resulting surface indentation are measured. This calibration is achieved by applying a series of CO₂ laser pulses to a sacrificial target made of the same or similar material to the one used during the iterative refinement milling, see Fig. 4. The pulses are spatially separated so that the indentation formed by each pulse is clearly resolved. The pulses are applied with varying duration but the same laser power. Each indentation is least-squares fit to a Gaussian, and the widths and height of the Gaussian are recorded. The iterative refinement algorithm interpolates the calibration data when calculating the set of pulse parameters which will minimize the mill error.

Initial error in calibration as well as additional variability due to uncontrolled thermal and mechanical effects relevant at the time scale of multiple milling iterations, change the material removal of a laser pulse. As this scales with the amount of material removed, these errors will approach the level of the constant errors as the measured surface converges to the target surface.

Experimentation with calibration has revealed that the volume of the material removed during a laser pulse depends on the gradient of the surface, as well as previous nearby ablations. This indicates a complex material response that precludes an effective single calibration and invites a lower than unity proportional gain to increase convergence stability.

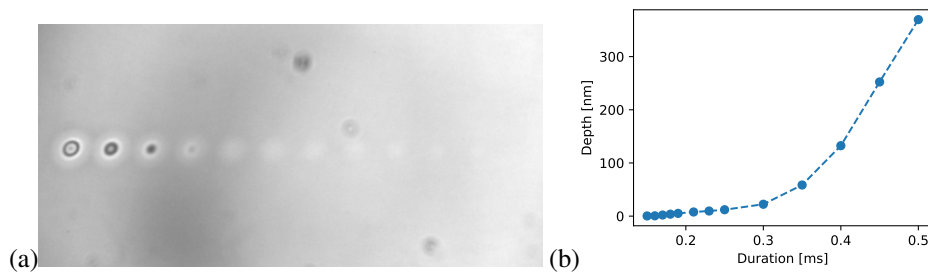


Fig. 4. (a) An example depth calibration showing milling spots from 13 pulses at a set power with durations varying between 150 μ s and 500 μ s. (b) The calibration curve generated from the milled array.

3.2.2. Pulse Duration Noise

The CO₂ laser is pulsed using an acousto-optic modulator (AOM). Although the timing noise does not depend on the duration of the laser pulse, the milling error caused by timing noise is proportional to the duration of the pulse. Due to the non-linear relationship between the pulse duration and volume of material removed (see Fig. 4), this error asymptotically approaches zero as the pulse duration approaches zero.

3.2.3. Laser Power Noise

The volume of material removed by a laser pulse strongly and non-linearly depends on the laser power. The milling apparatus uses a 5 W CO₂ laser (Access Lasers, model L5SLT-AOM), which produces approximately 1 W at the point of milling. In our current setup, iterative refinement with 10 – 15 iterations at a grid spacing of 3 μm over a 50 μm radius typically takes 1 – 2 hours, while the CO₂ laser power drifts on a time-scale of several minutes.

To monitor laser power, a pick-off, located down stream of the AOM, directs laser light onto a photodiode (Thorlabs, PDAVJ10). Software PID feeds back onto the AOM to stabilize the laser power. This is done both when the mill is idle, using a shutter located before the sample, as well as during milling. Uncontrolled thermal drifts in our photodiode are currently limiting the efficacy of PID stabilization.

3.3. Constant Errors

Constant errors do not scale with the amount of removed material and limit the final achievable surface error. They include: lower limit calibration error, laser pulse positioning error, optical profilometry measurement error, and the basis set limitations of a finite pulse grid.

3.3.1. Lower Limit Calibration Error

While the calibration error, as reported by the least-squares fit, is proportional to the volume of the Gaussian, this error is still present in, and limited by, the smallest measurable Gaussian indents we can achieve in calibration. This lower limit to calibration sets the minimum removable volume for the milling operation, limiting the minimum milling error.

3.3.2. Laser Pulse Position Error

Our system uses a 6-axis nanopositioner hexapod (SmarAct P-SLC-2) to manipulate the position of the sample relative to the CO₂ focal spot while the laser optics remain static. The hexapod achieves ±15 nm of position accuracy over 1 mm of travel, as well as ±10 μm rotational accuracy over the full rotational range. The hexapod can travel 79 mm along a single axis, which enables the target to move between CO₂ focus and an optical profilometer while maintaining sub-micrometer position accuracy. Choosing an appropriate stage acceleration is important to realize precise movements and reduce mechanical excitation induced positional errors.

The iterative refinement milling method requires precise targeting of specific surface locations as measured by the optical profilometer. Small positioning errors result in milling errors which do not decrease with milling iteration, while large offset errors result in the creation of a positive feedback loop leading to the destruction of the sample.

The offset between the location of the sample in the optical profilometer and the CO₂ focus is measured and updated through a process which we perform on each sample before milling. The sample surface is measured before and after firing a laser pulse targeting the center pixel in the optical profilometer imaging system. The resulting indentation is least-squares fit to a Gaussian, and corrections to the offset are extracted from the position fit parameters. As the iterative refinement milling method does not require a flat initial sample, the offset calibration is performed in situ on the mill sample. This calibration is often repeated a few times before beginning the milling process as this has been found to reduce the offset error. The offset between the optical profilometer and the laser focus does not significantly drift during sample loading or between milling runs.

To avoid random position error caused by vibrations, the mill is isolated from the environment using an actively controlled vibration stabilization platform along with an acoustic dampened and thermally stabilized enclosure.

3.3.3. Profilometry Measurement Error

Phase shifting interferometry (PSI) extracts profilometry data from interferograms by a Mirau imaging system. Phase shifting is achieved by translating the target, mounted directly to the hexapod stage, while a phase unwrapping algorithm [16] is used to calculate a surface profile. This is used to construct error maps to inform the parameters for the next milling iteration or for general calibration purposes. We primarily used the Hariharan algorithm [16] due to its simplicity and reasonable results.

Our custom built PSI system's resolution is limited by our camera resolution, interferometry wavelength, and choice of phase unwrapping algorithm. This effectively limits the minimum measurable RMS error to 200 pm, however, we observe single measurement errors closer to 5 nm, likely due to camera read noise. To address this, we take the average of 20 profile images to produce the profile used to generate the error maps for iteration, reducing this read noise to near 1 nm. We additionally are limited in the slope of surfaces which we can mill, ultimately by the Nyquist limit, constraining the arbitrariness of accessible geometries. As the pixel size of our camera is $0.28 \mu\text{m}$, and the single wavelength of our interferometry light is 477 nm, the steepest slope we could potentially resolve is roughly 40° . In practice our mill geometries are far shallower than this, and we have not rigorously tested more extreme cases.

3.3.4. Basis Set Limitations

Our feedback loop attempts to minimize errors by applying corrective Gaussian indentations to the measured surface at each milling grid point. The Gaussian parameters are fit from our depth calibrations (see Sec. 3.2.1). Due to the finite number of pulse dots in our grid, we do not have access to a complete basis required to analytically describe the target surface as a convolution of Gaussians. This will determine a limiting surface error value for a given geometry. This error is generally on the order of 100 pm for spherical surfaces, though will depend greatly on the grid density and the target surface.

3.4. Feedback Stability

During each refinement iteration, we remove a volume of material that is proportional to the error between the measured surface and the target surface. This proportional feedback gain is set to a value < 1 to prevent instability in the the feedback loop.

As we can only remove material, we don't see oscillations when the proportional feedback coefficient is too large. To correct errors that arise when too much material is removed, we adjust the height of the target surface so that all errors can be addressed by the removal of material, see Fig. 5. Therefore a modest and localized positive error, can necessitate that a large volume of material must be removed across the entire surface of the target. Consequently, a positive feedback can arise when the proportional feedback gain is set too high.

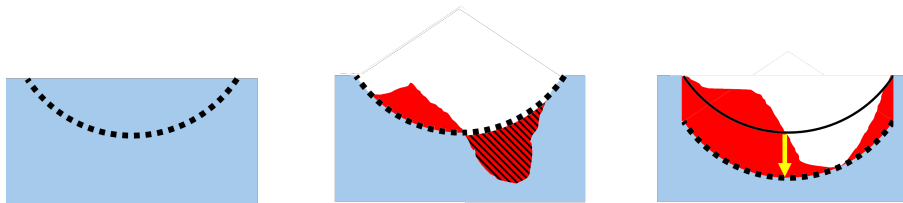


Fig. 5. When negative errors (hashed red region) are achieved by milling, our algorithm will shift the target fit down in space, as our system cannot add material to fill in negative errors. This shift enables a convergent approach to the target surface.

4. Results

We demonstrated milling individual spherical, multiple spherical, and conical axicon surfaces using our iterative refinement milling method. We show both phase profile images from our PSI as well as calculated residual error maps from representative mills for each design. We additionally demonstrate the ability to mill on various substrate materials, including fused silica slides, gradient index (GRIN) fibers, and coreless fibers.

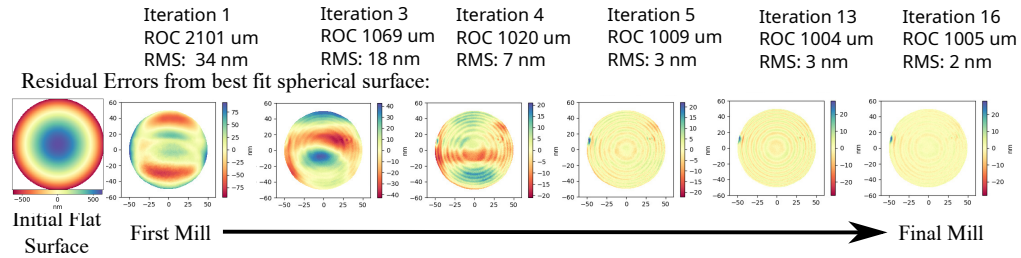


Fig. 6. Demonstration of the iterative milling of a 1 mm radius of curvature spherical surface on a fiber tip. The fiber was initially polished. The plots show the measured residual errors of the surface as compared to the exact target spherical surface.

4.1. Spherical Mirrors

Our iterative method has achieved target surface RMS of 2 nm on 100 μm diameter mirrors with 1 mm ROC on the tips of coreless fiber. This compares favorably with the 12 nm mean deviations reported by [11] using the dot-milling method for mirrors of similar parameters on a similar substrate. Fig. 6 shows the measured surface profile while applying iterative refinement milling to the tip of an optical fiber across 20 iterations. RMS values are calculated from our profilometry algorithms applied to the entire mirror surface. For high finesse cavities, the beam spot size at the mirror will be significantly smaller than the mirror diameter, indicating that surface error will be most impactful near the center of the mirror. When limited to a radius of 16 μm , roughly equivalent to the calculated beam spot size at the mirror for a confocal setup, our iterative milling process produces 100 μm diameter mirrors with RMS surface deviation of 0.77 nm. Identifying this small RMS with surface roughness corresponds roughly to a predicted finesse of $\mathcal{F} \approx 20000$ and an atom cooperativity of $\eta = 19.6$ in a confocal setup for our mirrors. We have not measured actual finesse for our mirrors. Results from finesse measurements on mirrors produced via dot-milling by [11] indicate surface roughness on the order of 0.3 nm, as determined through back-calculations of cavity losses from a reported finesse of $\mathcal{F} \approx 50000$.

4.1.1. Various Materials

We have successfully milled cavity mirrors into fused silica slides, coreless fibers (Thorlabs FG125LA), and GRIN fibers (Thorlabs GIF50C), see Fig. 7. Each of these targets exhibit different material responses to the milling process which are able to be accommodated for by our iterative method.

Milling GRIN fiber tips was explored due to mode-matching concerns in optical cavity applications. An appropriate length GRIN fiber spliced onto a single mode fiber acts as a lens, enabling tuning of the coupling into the fundamental mode of the cavity. This increases coupling efficiency by an order of magnitude.

We additionally attempted to mill on borosilicate glass slides. We found that the material response was drastically different from other targeted materials, demonstrating a limit to the immediate adaptability of our process to material properties. Initial mill attempts elicited material

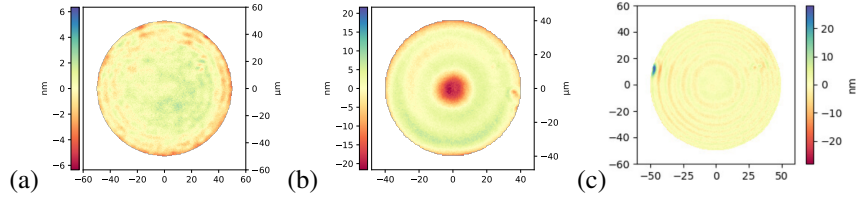


Fig. 7. (a) An example mill of a 1 mm ROC spherical surface on a glass slide, 1 nm RMS achieved after 25 iterations. (b) An example mill of a 1 mm ROC spherical surface on the tip of a GRIN fiber, 4 nm RMS achieved after 25 iterations. The material was more readily sculpted than coreless fiber or the glass slide, but our iterative method was able to accommodate and still produce a low roughness surface. (c) An example mill of a 1 mm ROC spherical surface on a coreless fiber tip, 2 nm RMS achieved after 16 iterations.

expansion without appreciable removal. Additional calibration and tuning of parameters may still enable successful milling of borosilicate.

Attempts to mill multi-mode (MM) fibers highlighted additional calibration complexities. The core and cladding regions of the fiber milled at significantly different rates, precluding effective milling across the boundary without further calibrations. This result is in agreement with dot-milling results on fibers with core in [11].

4.2. Demonstration of Arbitrary Surfaces

The signature strength of our iterative refinement milling method is the flexibility to quickly and efficiently produce optical surfaces with arbitrary geometries. We have modeled and fabricated several technically relevant examples to demonstrate this capability: narrow separation spherical mirrors in various configurations and axicon mirrors. Multiple spherical mirrors may enable evanescent coupled FFPCs for use in optical many-body cQED applications [17] whilst axicon mirrors can enable Bessel beam production for use in optical tweezing, optical vortex generation, etc. [18].

We milled closely spaced spherical mirrors with the goal of enabling coupled cavity arrays. Evanescent coupled arrays such as these can present many-body effects analogous to topological phases of matter, useful in exploring protected quantum phases for applications including quantum sensing and quantum computing [17]. The example geometry of a kagome lattice (tri-hexagonal tiling) was chosen as it presents topologically non-trivial band structures, both electronic as well as photonic.

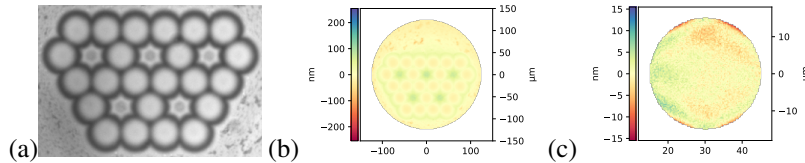


Fig. 8. (a) An example mill of a kagome lattice segment of 23 1.5 mm ROC 25 μm radius spherical surfaces on a fused silica slide. (b) The residual error of the resultant surface to the target surface, with 19 nm total surface RMS achieved after 30 iterations. (c) The residual error for a single component sphere, with 3 nm rms in the central 15 μm of each sphere.

In our initial testing, we produced a kagome lattice segment with 23 spherical mirrors, each

with a 1.5 mm ROC and a 25 μm radius, spaced with a 30 μm lattice constant. The resultant test structure was achieved in 30 iterations with a total RMS surface error of 19 nm as shown in Fig. 8. The RMS deviation of an individual mirror was 3 nm.

We additionally produced a 100 μm diameter conical axicon with an 87.5° half angle and 35 nm RMS error in 20 iterations. A significant portion of this surface error was attributable to limitations on the tip sharpness, as shown in Fig. 9. The approximately 7 μm radius rounded tip effectively limits the minimum input beam radius such that an appreciable portion of the beam will be translated into a Bessel beam. Slightly reducing the fit radius of the surface leads to an RMS of 10 nm, within an order of magnitude of focused ion beam milling fabrication quality [19].

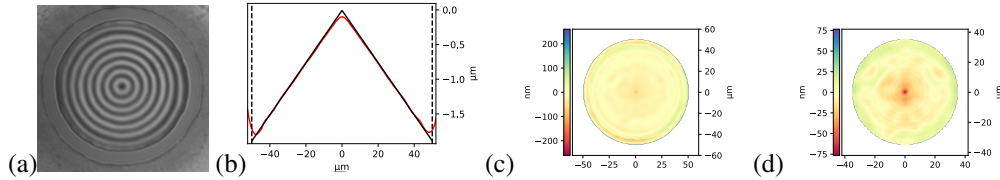


Fig. 9. (a) An 87.5° half-angle conical axicon milled into a fused silica slide, 35 nm total surface RMS achieved after 20 iterations. (b) Cross section of the axicon (red) comparing to target surface (black). (c) Residual error of the resultant surface to the target surface showing 35 nm RMS error. (d) Residual error when compared to a 35 μm reduced-radius target surface showing 10 nm RMS error; the error is dominated by the rounded tip.

Our current laser mill setup sets limitations for feature sizes, see Sec. 3.3.3, though this only limits the half-angle of the axicon cone to 40°. We have not yet tested the maximum achievable angle for this design.

5. Conclusions

We have demonstrated the capability to mill high quality, low roughness surfaces with arbitrary geometries on various materials, both on fiber tips as well as optical flats. We furthermore have shown the ability to do so using an agile, iterative method to dramatically reduce the time and effort needed to realize a desired surface. Our spherical surfaces were demonstrated to have lower RMS surface deviation than the dot-milling method. Although we have not measured finesses to back-calculate roughness, our current worst-case surface roughness measurements still afford sufficient predicted finesse for various applications. These results represent an improvement in manufacturing efficiency and quality over existing technologies, and a capability to generate manifold tools for cold atom manipulation and cQED applications.

This work was funded by the Air Force Office of Scientific Research under lab task 22RV-COR017.

We would like to thank Professor Chandra Raman and Jacob Williamson for their very useful discussions which were helpful in ferreting out technical challenges. We additionally would like to thank Logan Mamanakis for his assistance upgrading the apparatus.

Disclaimer

The views expressed are those of the authors and do not necessarily reflect the official policy or position of the Department of the Air Force, the Department of the Defense, or the U.S. Government. The authors declare no conflicts of interest. Data underlying the results presented in this paper are not publicly available at this time but may be obtained from the authors upon reasonable request.

References

1. C. M. Miller and F. J. Janniello, "Passively temperature compensated fibre fabry-perot filter and its application in wavelength division multiple access computer network," *Electron. Lett.* **26** (1990).
2. C. Toninelli, Y. Delley, T. Stöferle, *et al.*, "A scanning microcavity for in situ control of single-molecule emission," *Appl. Phys. Lett.* **97** (2010).
3. M. Mader, J. Reichel, T. W. Hänsch, and D. Hunger, "A scanning cavity microscope," *Nat. Commun.* **6** (2015).
4. J. Ma, Y. S. S. Patil, J. Yu, *et al.*, "A proposal for detecting the spin of a single electron in superfluid helium," arxiv preprint (2023).
5. E. S. Cooper, P. Kunkel, A. Periwal, and M. Schleier-Smith, "Graph states of atomic ensembles engineering by photon-mediated entanglement," *Nature* **20** (2024).
6. H. Pfeifer, L. Ratschbacher, J. Gallego, *et al.*, "Achievements and perspectives of optical fiber fabry-perot cavities," *Appl. Phys. B* **128**, 29 (2022).
7. P. Qing, J. Gong, X. Lin, *et al.*, "A simple approach to fiber-based tunable microcavity with high coupling efficiency," *Appl. Phys. Lett.* **114**, 021106 (2019).
8. A. A. P. Trichet, P. R. Dolan, D. M. Coles, *et al.*, "Topographic control of open-access microcavities at the nanometer scale," *Opt. Express* **23**, 17205–17216 (2015).
9. D. Hunger, T. Steinmetz, Y. Colombe, *et al.*, "A fiber Fabry-Perot cavity with high finesse," *New J. Phys.* **12**, 065038 (2010).
10. T. Ruelle, M. Poggio, and F. Braakman, "Optimized single-shot laser ablation of concave mirror templates on optical fibers," *Appl. Opt.* **58**, 3784–3789 (2019).
11. K. Ott, S. Garcia, R. Kohlhaas, *et al.*, "Millimeter-long fiber fabry-perot cavities," *Opt. Express* **24**, 9839–9853 (2016).
12. Y. Colombe, T. Steinmetz, G. Dubois, *et al.*, "Strong atom-field coupling for bose-einstein condensates in an optical cavity on a chip," *NATURE* **450**, 272–U9 (2007).
13. N. Ismail, C. C. Kores, D. Geskus, and M. Pollnau, "Fabry-perot resonator: spectral line shapes, generic and related airy distributions, linewidths, finesse, and performance at low or frequency-dependent reflectivity," *Opt. Express* **24**, 16366 (2016).
14. H. Bennett, "Scattering characteristics of optical materials," *Opt. Prop. Opt. Mater.* **17** (1978).
15. M. Motsch, M. Zeppenfeld, P. W. H. Pinsky, and G. Rempe, "Cavity-enhanced rayleigh scattering," *New J. Phys.* **12** (2010).
16. J. H. Bruning, A. Cornejo-Rodriguez, K. Creath, *et al.*, *Optical Shop Testing* (John Wiley and Sons, Inc., 2007), 3rd ed.
17. A. J. Kollár, M. Fitzpatrick, P. Sarnak, and A. A. Houck, "Line-graph lattices: Euclidean and non-euclidean flat bands, and implementations in circuit quantum electrodynamics," *Commun. Math. Phys.* **376**, 1909–1956 (2019).
18. S. Khonina, N. Kazanskiy, S. Karpeev, and M. Butt, "Bessel beam: Significance and applications – a progressive review," *Micromachines* **11** (2019).
19. S. Cabrini, C. Liberale, D. Cojoc, *et al.*, "Axicon lens on optical fiber forming optical tweezers, made by focused ion beam milling," *Microelectron. Eng.* **83**, 804–807 (2006).